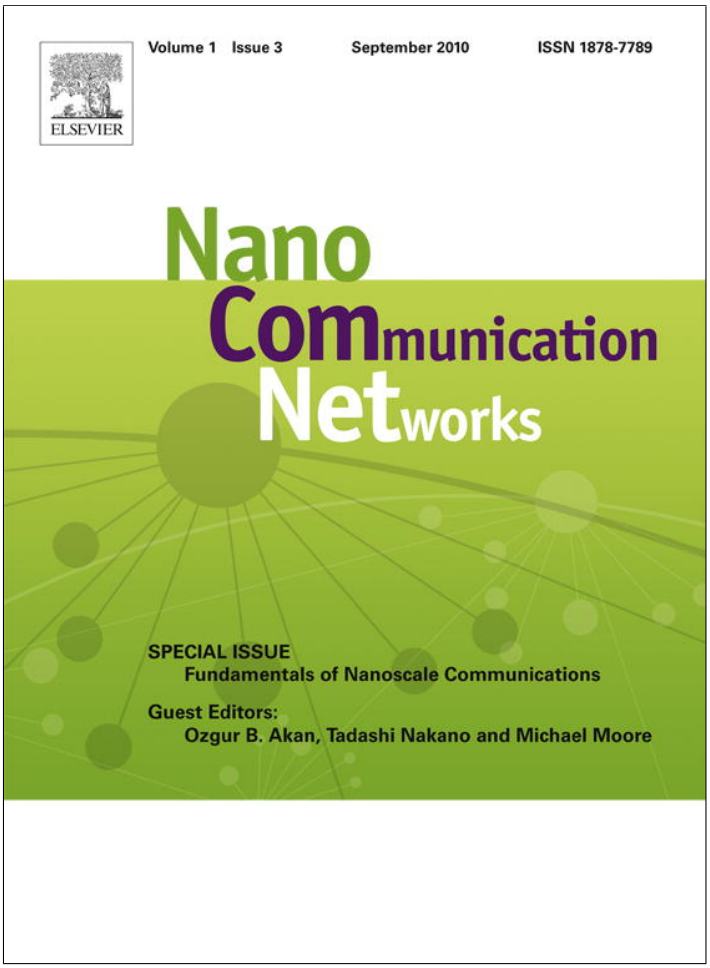

Nano Communication Networks 1 (2010) 160–172

Contents lists available at ScienceDirect

Nano Communication Networks

journal homepage: www.elsevier.com/locate/nanocomnet

Design and analysis of systems based on RF receivers with multiple carbon nanotube antennas

C. Emre Koksal, Eylem Ekici *, Siddharth Rajan

Department of Electrical and Computer Engineering, The Ohio State University, Columbus, OH, United States

ARTICLE INFO

Article history:
Received 9 July 2010
Accepted 2 September 2010
Available online 15 October 2010

Keywords:
Nanocommunication
Nanoscale networks
Carbon nanotube receivers
CNT-antenna-based systems

ABSTRACT

In this paper, possible uses of systems composed of multiple CNT-based EM receivers are introduced and their communication-theoretical analysis developed. Four possible example applications that involve multiple CNTs are discussed and their system-level design is emphasized. Then, a communication-theoretical analysis of the performance of a generic system that involves multiple CNT-based RF receivers is introduced. The generic receiver system in question is the underlying component of the example applications and their system-level design. Furthermore, the analysis provides some insights into fundamental questions such as communication rate and encoding of information in nanoscale devices.

1. Introduction

Nanoscale systems are envisioned for many crucial future applications ranging from targeted medicine and drug delivery to high fidelity sensors [1,7–9,3]. Effectiveness and application domains of nanoscale systems can increase by leaps and bounds when such systems can interact with each other through wireless communication. Miniaturization of communications systems has been in the forefront of research and development efforts for decades. Until very recently, communication system sizes and design alternatives were considered limited by the circuit, battery, and most importantly, antenna sizes. For instance, the use of common operating frequencies of hundreds of MHz to several GHz meant an antenna size in the order of centimeters. Such limitations render the incorporation of communication into nanoscale systems impossible. Electromagnetic communication in such scales is reserved for the THz range, which has extremely high attenuation through matter [13]. Therefore, traditional EM-based communication had very limited use in nanoscale devices and systems. Instead, other paradigms were considered to facilitate communication of nanoscale devices [1,15]. Most notably, molecular communication [15] has been proposed to exchange messages between nanoscale devices over short distances through a diffusion process. For longer distances, more active modes of communication are considered such as through moving bacteria [10,4].

Recently, new EM-based radio receivers and transmitters have been proposed using *carbon nanotubes (CNTs)* [12,19]. These communication systems are fundamentally different from traditional antenna-based systems: Rather than relying on the oscillation of electrons inside the antenna in response to EM waves, CNTs oscillate themselves when they are charged. Oscillations lead to variation of the distance of the tip of the CNT from a cathode plate. The distance variations are then detected as fluctuations of the emission current. CNT-based receiver systems have been validated in implementation [12] and further analyzed in [6]. The ground-breaking property of CNT-based communication systems is that it is possible to establish communication in the hundreds of MHz range with systems that are hundreds of nm in size. Even more recently, we have developed a communication-theoretical analysis of CNT-based receiver systems [14]. Almost concurrently, system and networking aspects of nanoscale devices with

* Corresponding author. Tel.: +1 614 292 0495; fax: +1 614 292 7596.
E-mail addresses: koksal@ece.osu.edu (C. Emre Koksal), ekici@ece.osu.edu, ekici.2@osu.edu (E. Ekici), rajan@ece.osu.edu (S. Rajan).

1878-7789/$ – see front matter © 2010 Elsevier Ltd. All rights reserved.
doi:10.1016/j.nancom.2010.09.001

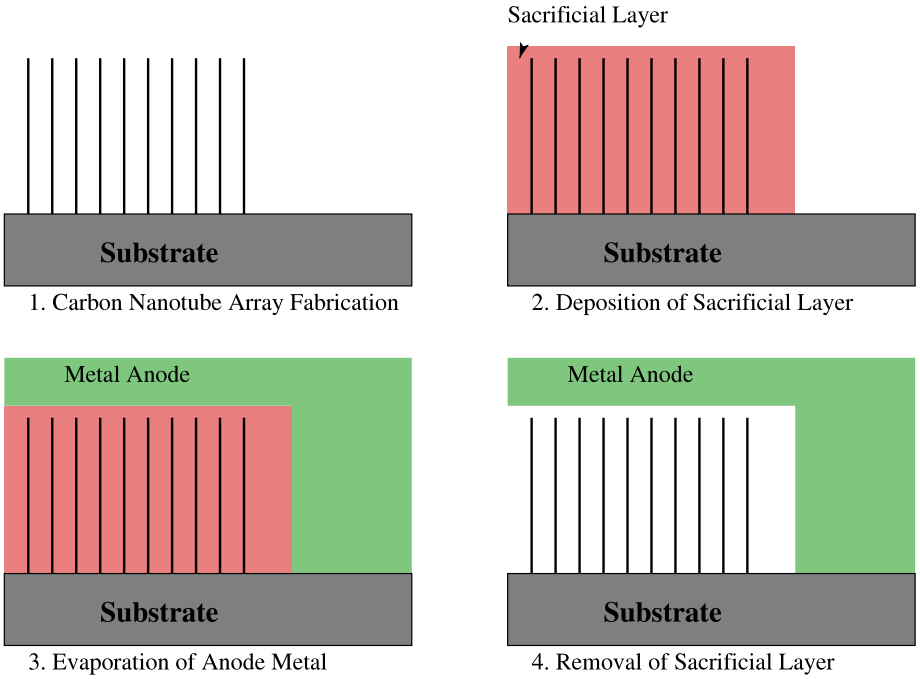

Fig. 1. Fabrication process [11].

CNT-based radios have been discussed in [2]. The promising nature of CNT-based communication (sub)systems is also evident in this and other recent research activities.

Furthermore, recent advances in nanotube fabrication have enabled commercial fabrication of arrays of CNTs with good control of density, diameter and length of the CNTs. One possible fabrication process is shown in Fig. 1. In Step 1, a CNT array is fabricated on a substrate. A sacrificial layer is then deposited, followed by evaporation of the anode metal. The sacrificial layer is then removed using a wet etch step, leading to a suspended anode field emitter structure as shown. Other versions, such as a deposition of a "grid" metal are also possible. The main challenge in the fabrication process is maintaining the a short distance between the CNT tip and anode terminal. This distance is limited by the variance in length of the CNT and control of the fabrication process.

In this paper, we aim to introduce possible uses of systems composed of *multiple* CNT-based EM receivers and develop their communication-theoretical analysis. We discuss four possible example application areas that involve multiple CNTs. In this part, we emphasize the applications and their system-level design. We then introduce a communication-theoretical analysis of the performance of a generic system that involves multiple CNT-based RF receivers. The generic receiver system in question is the underlying component of the example applications and their system-level design. Furthermore, the analysis provides some insights to the questions set forth in [2], such as communication rate and encoding of information. Finally, we discuss possible open research problems and conclude this paper.

2. Applications of CNT-based RF receiver systems

In this section, we discuss several systems that can be built using CNT-based RF receiver systems. These applications leverage the frequency-selective tunneling response of CNTs to accomplish tasks that are not realizable at such small scales. At the heart of all these applications lies the basic principle of CNT-based receivers: The field emission current fluctuates as the CNT oscillates due to externally received EM radiation. A CNT responds to carriers at a certain frequency, which is referred to as the *resonance frequency* of the CNT. The resonance frequency of a CNT depends on its length, as well as other factors. Hence, using CNTs of different lengths allows us to *query* the CNT forest for spatial and temporal changes. In what follows, four possible applications are highlighted, namely deformation measurements of nanoscale 2D surfaces, CNT length distribution measurement, particle detectors, and nanoscale RF receivers.

2.1. Nanoscale 2D deformation measurements

The basic structure of the proposed 2D flexing measurements consists of a fixed cathode plate and an anode plate on which CNTs of varying lengths are planted. The anode plate is fixed in *one corner*, creating a cantilever type surface, allowing for flexing of the anode along two dimensions. As the anode flexes, the distance of the CNTs to cathodes change, as well. This clearly affects the field emission current measured in the system.

The main problem with this basic system is that various types of bends can lead to the same measurement of the current. However, in our design, the CNTs are arranged in increasing length along two dimensions as shown in Fig. 2. EM bursts of matching resonance frequencies of CNT lengths deployed are used to excite different groups of CNTs of similar lengths. With every EM burst, it is possible to observe the differential changes in the emission current that can be mapped to the distance of CNTs that are excited from the cathode. With the a priori knowledge of the distribution of CNT lengths on the anode, one can map the deformation of the cantilever surface in two dimensions.

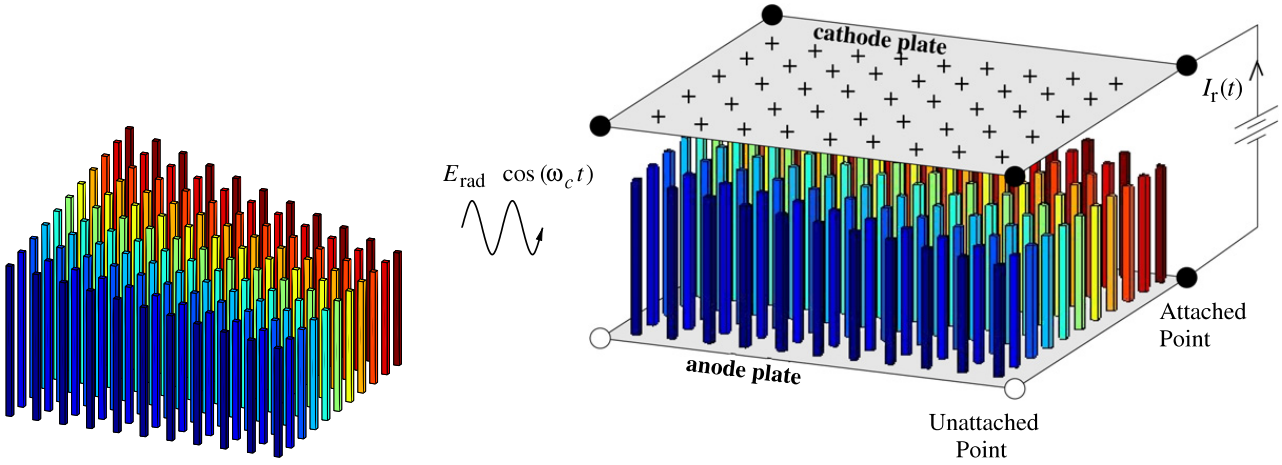

(a) Distribution of CNT lengths. (b) System overview.

Fig. 2. Nanoscale 2D deformation measurement setup.

2.2. CNT length distribution

CNTs are considered as ideal field emission devices, especially for flat-panel displays. During the process of growing the CNT forests, it is highly probable that CNTs of various lengths would be deposited on the surface of a substrate rather than CNTs with identical lengths. Furthermore, the density of CNTs may vary on this 2D space. This may lead to varying field emission intensity on (potentially) large surfaces. While it is beyond the scope of this article to comment on how uniformity in CNT density and length can be achieved, we do provide a means to characterize such CNT forests. This knowledge can be used to identify whether the manufactured field emission device conforms to quality standards.

Using a constant voltage between the anode plate on which the CNT forest resides and a small probe serving as the cathode that moves close to the anode plate, it is possible to measure the combined field emission effect of the spatial density and length distributions of CNTs. However, combining this basic setup with EM waves at various carrier frequencies, we can probe the area under the probe for the reaction of CNTs that respond to a certain carrier frequency. An example system has been shown in Fig. 3. Moving the tip of the probe across the entire surface and, at each location tested, collecting current variations as we scan a range of carrier frequencies, we can develop a *map of CNT lengths and their densities* over a large surface area.

2.3. Particle detector

It is also possible to use CNT-based RF receiver systems to detect the presence of micro-scale particles in the environment. The main idea is to create a lattice of CNTs grouped according to their lengths, where shorter CNTs are placed more densely together and longer ones more sparsely. Since the amplitude of CNT oscillations is in the order of its length, such lengths also correspond to their spacing. The idea is to place the particle detector behind a filter that allow only particles below a certain size through. When particles penetrate the filter and

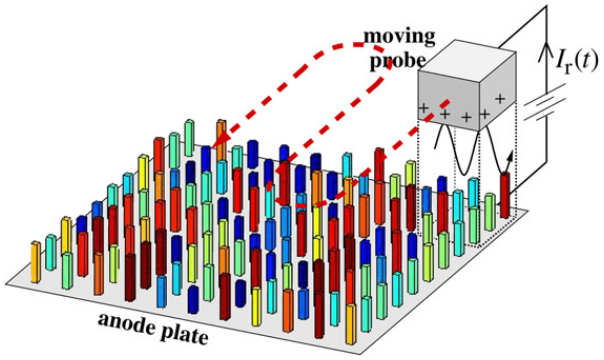

Fig. 3. Spatial CNT length distribution measurement system.

lodge on the anode surface, they block the movement of some CNTs and hence we can *query* each group of CNTs, exciting them with EM carriers at appropriate frequencies and observing the response. An example system is depicted in Fig. 4. In this example, the anode is seeded with CNTs of three length groups that correspond to resonance frequencies of $f_{0,1}, f_{0,2}$, and $f_{0,3}$. The particles (depicted as spheres) land on the surface of the anode, they block the oscillations of shorter length CNTs with higher probability. Since the spacing of longer CNTs is larger, as well, they can reside between CNTs without adversely affecting their oscillations. The detector works by scanning the appropriate resonance frequencies and observing the changes in the field emission current. A highly impeded response to an EM wave of center frequency f_0 suggests that the particles are greater than or equal to the spacing for the corresponding group of CNTs. In the example of Fig. 4, frequency responses to $f_{0,1}$ and $f_{0,2}$ are impeded since the particles prevent them from freely oscillating. On the other hand, if the response does not change significantly with respect to particle-free operation, this suggest that particles are either not present or smaller than the spacing for that group of CNTs. In the same example, the particles are lodged between long CNTs with resonance frequency $f_{0,3}$ and therefore do not affect the oscillations of the longest group of CNTs. As such, the proposed detector does not only detect the presence of particles, but also provides an estimate of their sizes.

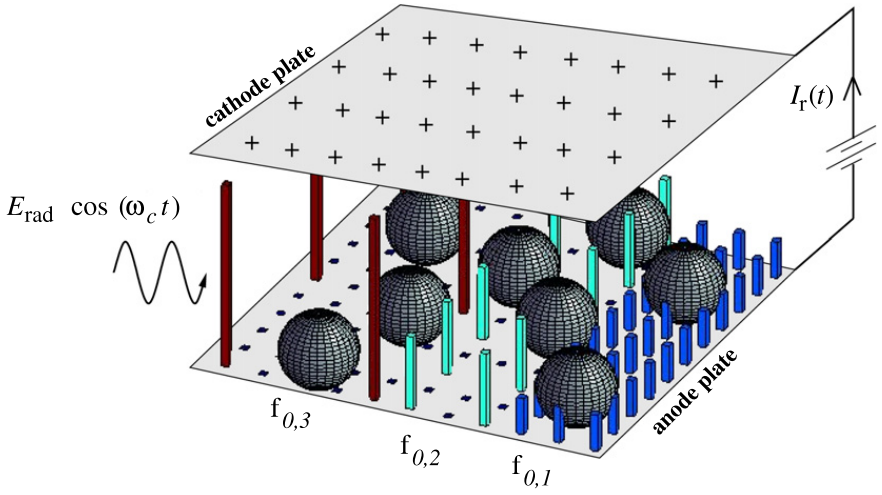

Fig. 4. Particle detector.

Another version of a particle detector can be designed whereby the objective is not only to detect the presence of particles of certain sizes, but to actually *locate* them on the sensor's surface. To accomplish this, the basic structure of Fig. 4 is modified such that the cathode plate is partitioned into k sectors, each of which is connected to a different detector. Without barring other possibilities, we assume that a relatively uniform CNT length distribution is assumed throughout the anode's surface. Each sector measures the current induced by n/k CNTs. When particles of a certain size are present, the oscillations of CNTs in that sector are obstructed, which is picked up by the dedicated receiver mechanism.

2.4. Nanoscale RF receivers

A direct application of systems in question is their use as RF receiver systems. In contrast to regular RF detection methods, the mechanical oscillations of CNTs allow the detection of EM radiation of low frequencies (in the order of hundreds of MHz) at the nanoscale. At this scale, traditional methods of RF detection occur in the THz range. The main advantage of such systems is immense capability for miniaturization in the receiver's design. Since the CNT-based receivers readily "demodulate" transmissions, it is also a low cost and low power system. The main challenge in such systems is to overcome the requirement of high SNR to achieve low error rates. The parallel use of multiple CNTs with similar sizes allows us to tackle this dilemma easily. In such systems, the main challenges are associated not with the theoretically achievable performance limits, but with the random distribution of CNT lengths. In the following section, we will focus on nanoscale RF receivers and present their systematic analysis.

3. Physical model

3.1. Basics of CNT response to EM radiation

Previous work on CNTs as electromechanical actuators has shown that CNTs behave like cantilevers with high elastic strength, and an elastic constant in the 100 GPa range [16]. A longitudinal electric field applied on a CNT induces a charge density at the tip of the CNT [11]. A anode terminal placed above the CNT causes a charge to be induced, and the magnitude of the charge is proportional to the field applied. If an electric field is applied to this *perpendicular* to the axial direction, the CNT also experiences a bending force due to the charge at its tip. Under electromagnetic excitation, the oscillating electric field perpendicular to the CNT would exert an oscillating force on it and cause it to move. If the frequency is chosen to be near the resonance frequency of the CNT cantilever, then electromagnetic energy couples most efficiently into the CNT, and the CNT vibrates with a large amplitude at its natural resonance frequency. Experimental work has confirmed this model for the coupling of electromagnetic radiation into CNTs through direct observation of the nanotube bending [16].

We make several simplifying assumptions in our model for the CNT antenna. Firstly, similar to [16,12], we assume that the charge is localized at the tip. While the position and magnitude of this charge affects the amplitude of vibration, fundamental properties such as mass, length, and diameter determine the resonance frequency and quality factor (Q) of the cantilever vibration. Therefore, for small vibrations, the response curves of a CNT would be independent of the charge on the tip, except for a constant multiplier. Based on the aforementioned assumptions, a simple theoretical model for electromagnetic excitation of CNTs was provided by Jensen et al. [12]. There, the CNT was modeled as a cantilever with a characteristic vibration frequency, f_c, given by

$$f_c = \frac{0.56}{L^2}\sqrt{\frac{YI}{\rho A}}, \tag{1}$$

where L and A re the length and area of the nanotube, Y is the Young's modulus, ρ is the density and I is the real moment of inertia ($I = \pi/4(r_o^4 - r_i^4)$ for a cylinder with outer and inner radii of r_o and r_i respectively). The amplitude of vibration of such a cantilever is

$$y = \frac{qE_{rad}/m_{eff}}{4\pi^2\sqrt{(f^2 - f_c^2)^2 + (ff_c/Q)^2}}, \tag{2}$$

where E_{rad} is the amplitude of the radiant electric field, m_{eff} is the mass of the cantilever, f_c is the resonant oscillation frequency, and Q denotes the value of the Q-factor of the cantilever vibrations.

Fowler–Nordheim quantum mechanical tunneling has been shown [5] to be the basis for field emitters based on CNTs. The concentration of the electric field at the tip of the CNT leads to a very high field intensity, and enhances the field-assisted tunneling of electrons from the tip of the CNT to the anode. As the CNT oscillates, the distance between the tip of the CNT and the anode varies. The tunneling current varies exponentially with the distance between the tip and the anode, given by the Fowler–Nordheim equation:

$$I = c_1 A(\gamma E_{\text{ext}})^2 \mathrm{e}^{-\frac{c_2}{\gamma E_{\text{ext}}}}, \tag{3}$$

where c_1 and c_2 are constants that depend on the geometry of the device, A is the area from which the CNT emits electrons, E_{ext} is the external applied electric field, and γ is a "field enhancement factor" that depends linearly on the distance between the tip and the anode. The combination of field-assisted tunneling (used commonly in vacuum emitters) with the electromechanical bending of CNTs enables amplification of the electromechanical effect, much like any other three-terminal electron device such as a bipolar junction transistor or a field effect transistor. Since the tunneling current depends exponentially on the inverse of the distance, small deviations of the CNT due to bending can lead to large changes in the tunneling current. Typically, the amplitude, y, of the vibrations is small compared to the length L of the CNT. Thus, as detailed in [12,14], the second order term in the Taylor series expansion of I (given in (3)) is the dominant term and the amplitude of fluctuations in the current (observed signal) is proportional to $|y|^2$. This leads to a square-law behavior for the observed signal, with respect to the incident radiant electric field strength.

Note that, the described electromechanical interaction behaves like the base (BJT) or gate (FET) for a transistor and changes the output tunneling current exponentially. This is the basis for gain in the device. An important point of difference from a normal amplifier is that in this device, the input is already matched to provide maximum gain at the natural resonance frequency. The circuit equivalent of this would be a transistor with a narrow band-pass filter with high Q. The responsivity of the CNTs to incoming radiation increases with the applied field between the anode and the CNT cathode since the amount of charge induced at the tip, as well as the tunneling current increase.

Further assumptions we make in our physical model of CNTs are the following. First, the distance between the CNT tip and anode terminal differs from one CNT to another due to the variations in the length L of the CNT caused by the imperfections of the fabrication process. Consequently, we model center frequency f_c, which is a function of L as a random variable. Another issue that is important for arrays of CNTs is the non-uniformity of the transverse electromagnetic field. Since the CNT arrays are high aspect ratio (height/width) structures, electromagnetic fields would be scattered, and the transverse electromagnetic field intensity may have variations (both of amplitude and phase) within an array due to scattering. This effect is not taken into account in our model; accurate determination would require a three-dimensional calculation of the electromagnetic properties of the system. However, we note that for the relatively long wavelengths of interest ($\sim$10 cm) and the small size of the arrays ($\sim$100 μm), the variation in electric field intensity will be rather small.

3.2. Nanoreceiver model

With the aforementioned assumptions, our nanoreceiver is a generalization of the architecture we proposed in [14], where each node contained a single antenna. The abstract model for our *multiantenna* nanoreceiver is given in Fig. 5. The basic components of the *front end* include n nanoantennas and n associated square-law devices. Here, $h_{\text{r},j}(t)$ is the impulse response of the linear filter that captures the input–output behavior of the jth nanoantenna, where the input $Y_{\text{i},j}(t)$ is the incoming electromagnetic field and the output $Y_{\text{o},j}(t)$ is the amplitude of the associated vibrations. Based on the physical model given in the previous section, the frequency response of the jth nanoantenna can be found to be:

$$H_{\text{r},j}(f) = \frac{|Y_{\text{o},j}(f)|}{E_{\text{rad}}(f)} = \frac{q/m_{\text{eff}}}{4\pi^2\sqrt{(f^2 - f_{\text{c},j}^2)^2 + (ff_{\text{c},j}/Q)^2}}, \tag{4}$$

where $f_{\text{c},j}$ is the resonance frequency of the jth nanoantenna. We assume the length of each nanoantenna (and hence its associated resonance frequency) to be random. We model this randomness using a normal distribution,[1] i.e., $f_{\text{c},j} \sim \mathcal{N}(f_0, \sigma_{f_0}^2)$, independently of $f_{\text{c},j'}$ for all $j' \neq j$. Here, f_0 is the mean center frequency and $\sigma_{f_0}^2$ represents the variability of the center frequency due to the variability in the antenna length. We assume that

$$\sigma_{f_0} \ll f_0 \tag{5}$$

and therefore the gains of the filters at their respective resonance frequencies are approximately identical, i.e.,

$$H_{\text{r},j}(f_{\text{c},j}) \approx \frac{q/m_{\text{eff}}}{4\pi^2 f_0^2/Q} \triangleq H_{\text{res}}, \tag{6}$$

for all $j \in \{1, \ldots, n\}$. Since the response of each antenna j is symmetric with respect to its resonance frequency $f_{\text{c},j}$, the 3-dB bandwidth, B, of $H_{\text{r},j}(f)$ can be found by solving $H_{\text{r},j}(f_{\text{c},j})/\sqrt{2} = H_{\text{r},j}(f_{\text{c},j} + B)$. With the additional assumption that

$$B \ll f_0, \tag{7}$$

one can find $B \approx \frac{f_0}{2Q}$ for all the antennas. Note that, Assumptions (5) and (7) are highly accurate for typical values of Q (i.e., between 100 and 1000) and f_0 (i.e., between 10 and 500 MHz). Finally, we use the square-law device at each branch due to the fact that the observed current, $I_{\text{r},j}(t)$ is proportional to the square[2] of the amplitude of the vibrations of the nanotube.

The signal is corrupted by additive white Gaussian noise (AWGN) at two levels: The *acoustic noise*, $W_{\text{a},j}(t)$, is

[1] The subsequent analysis can also be generalized to arbitrary distributions of $f_{\text{c},j}$.

[2] Note that the detected current is proportional to the square of $\Delta\gamma(t)$, which in turn is proportional to the amplitude $|Y_{\text{o},j}(t)|$.

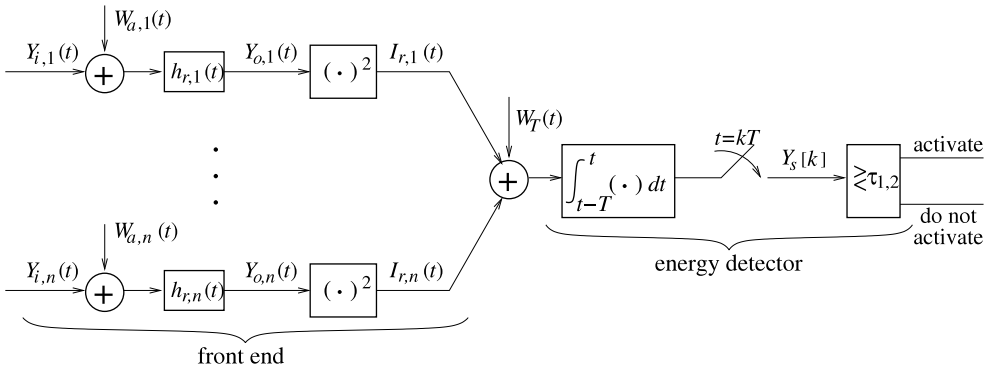

Fig. 5. System model of our nanoreceiver.

the mechanical component that affects the amplitude of the vibrations $Y_{o,j}(t)$, whereas the *thermal noise*, $W_T(t)$ is added to the total detected current. We denote the two sided power spectral densities of the acoustic noise and the thermal noise with $N_a/2$ and $N_T/2$ respectively.

For a nanoreceiver to be feasible, low complexity is one of the main constraints. At the nanoscale, even slightly complex components become infeasible. Hence, to achieve node activation, we use the same simple energy detector as in [14], as shown in Fig. 5. Since the signal $\sum_{j=1}^{n} I_{r,j}(t)$ is the current at the output of the front-end of the receiver, the integrator can be realized by a mere *capacitor*. The integrator is followed by the sampler, sampling the output of the integrator once every T seconds, which we refer to as the *activation period*. We assume that the activation period is much longer than the reciprocal of the 3-dB bandwidth of the antenna response. Hence, we have:

$$\frac{1}{T} \ll B. \tag{8}$$

We shall verify this assumption later, in Section 4. Finally, each sample $Y_s[k]$ is compared with a pair of predetermined thresholds τ_1 and τ_2 (as will be explained in the next section) and the node becomes active depending on these comparisons.

The combination of the square-law devices at each branch and the integrator acts as a *demodulator* for each waveform $Y_{o,j}(t)$ separately. However, note that, $Y_{o,j}(t)$ also includes the noise component $W_{a,j}(t)$, filtered by the antenna response $h_{r,j}(t)$. Since we do not have any front-end filter to remove the out-of-band noise components, the performance of the system degrades. This is the price paid to avoid realizing the filter. Notice that, in our energy detector, the only components we used are a capacitor, a sampler and a series of comparators.

4. Node activation with multiple antennas

In this section, we present a communication theoretic analysis of our receiver, given in Fig. 5. In particular, we will provide tradeoffs among number of antennas, signal to noise ratio, probability of error and the time required for activation.[3] Note that the analyses in this section are generalizations of the single antenna analyses of [14]. For completeness, we repeat the basics here.

To activate a node, we assume that the activator uses pure sinusoids of duration T. Since the size of the cathode, on which all CNTs lie is much smaller than the typical wavelengths (RF range), we assume no phase difference among the input signals observed at different antennas. Consequently, at the input of each nanoantenna j, we have $Y_{i,j}(t) = Y_i(t) = a\cos(2\pi f_0 t + \phi)$, where ϕ is the random phase. It is the most energy-efficient way of activating a node to choose the frequency of the sinusoid, identical to the mean resonance frequency f_0 of the nanoantennas. We also address the issue of mismatch between the frequency of the carrier and the mean resonance frequency of the antennas later on. The signal at the output of antenna j is:

$$Y_{o,j}(t) = \begin{cases} a\cos(2\pi f_0 t + \phi)|H_{r,j}(f_0)| + \tilde{W}_{a,j}(t), \\ \quad \text{activation attempt} \\ \tilde{W}_{a,j}(t), \quad \text{otherwise}, \end{cases} \tag{9}$$

where $H_{r,j}(f)$ is the frequency response of the jth nanoantenna and the acoustic white Gaussian noise, filtered by the antenna response is denoted by $\tilde{W}_{a,j}(t)$, which is also a Gaussian process. Hence, the pre-thermal noise portion of the current at the output of the jth branch of the front-end of the receiver can be written as

$$I_{r,j}(t) = \begin{cases} a^2|H_{r,j}(f_0)|^2\cos^2(2\pi f_0 t + \phi) + 2a|H_{r,j}(f_0)| \\ \quad \times \cos(2\pi f_0 t + \phi)\tilde{W}_{a,j}(t) + \tilde{W}^2_{a,j}(t), \\ \quad \text{activation attempt} \\ \tilde{W}^2_{a,j}(t), \quad \text{otherwise}. \end{cases} \tag{10}$$

The energy detector integrates $\sum_{j=1}^{n}(I_{r,j}(t)) + W_T(t)$ over the past T seconds and a sampler samples the output of the integrator every T seconds. We initially disregard the issue of timing and carrier frequency mismatch between the activator and the nanoreceiver in the following analysis, but study carrier frequency mismatch later on. The impact of these imperfections was addressed in [14] in depth, where the (single) antenna resonance frequency is a deterministic constant. Here $H_{r,j}(f_0)$ is a random variable, which is a function of the random resonance frequency $f_{c,j}$ of the each antenna.

One can realize that there are three components of $I_{r,j}(t)$ under the activation attempt, as given in Eq. (10). The first one is the *signal component*, the second one is the *signal–noise cross component*, which is a Gaussian process,

[3] A generalization of node activation to more complex digital communication is discussed throughout the section where appropriate.

and the last one is the *noise–noise cross component*, which has Chi-squared samples. Next we analyze the contribution of each component as well as the thermal noise to the detected sample $Y_s[1]$ under an activation attempt in the first activation period $k = 1$:

(1) *Signal component*: Given an activation attempt in the scheduling period $k = 1$, the signal component of $Y_s[1]$ can be written as:

$$Y_s^{(s)}[1] = \sum_{j=1}^{n} \int_0^T a^2 |H_{r,j}(f_0)|^2 \cos^2(2\pi f_0 t + \phi)\, dt = \frac{1}{2} T a^2 \sum_{j=1}^{n} |H_{r,j}(f_0)|^2. \quad (11)$$

Note that phase recovery comes for free due to the square-law device over each branch, and hence our nanoreceiver avoids the associated complex circuitry for that task.

One can observe that,

$$\frac{|H_{r,j}(f_0)|^2}{H_{res}^2} \approx \frac{f_0^4/Q^2}{f_0^4/Q^2 + 4f_0^2(f_{c,j} - f_0)^2} = \frac{1}{1 + (f_{c,j} - f_0)^2/B^2}, \quad (12)$$

where (12) follows from (6), (5) and that $B \approx \frac{f_0}{2Q}$. Defining

$$a_{eff}^2 \triangleq a^2 \frac{1}{H_{res}^2} \sum_{j=1}^{n} |H_{r,j}(f_0)|^2, \quad (13)$$

we can rewrite the signal component as:

$$Y_s^{(s)}[1] = \frac{1}{2} T a_{eff}^2 H_{res}^2. \quad (14)$$

Note that, if $\sigma_{f_0}^2 \ll B$, then $[1 + (f_{c,j} - f_0)^2/B^2]^{-1} \approx 1 - (f_{c,j} - f_0)^2/B^2$ with high probability. In that case, a_{eff}^2 will have an nth order Chi-squared distribution. Also, for a large number of CNTs, i.e., $n \gg 1$,

$$\frac{a_{eff}^2}{n} = \frac{a^2}{H_{res}^2} \cdot \frac{1}{n} \sum_{j=1}^{n} |H_{r,j}(f_0)|^2 \approx \frac{a^2}{H_{res}^2} \cdot \mathrm{E}\left[|H_{r,1}(f_0)|^2\right] = \frac{\mathrm{E}\left[a_{eff}^2\right]}{n} \quad (15)$$

with high probability from the strong law of large numbers, where the expectation is over the joint distribution of $f_{c,1}, \ldots, f_{c,n}$.

(2) *Signal–noise cross component*: Given an activation attempt in scheduling period $k = 1$, the signal–noise cross component can be written as:

$$Y_s^{(s-n)}[1] = \sum_{j=1}^{n} \int_0^T 2a|H_{r,j}(f_0)| \cos(2\pi f_0 t + \phi) \times \tilde{W}_{a,j}(t)\, dt. \quad (16)$$

Since $\tilde{W}_{a,j}(t)$ is a Gaussian process, $Y_s^{(s-n)}[1]$ is a conditionally Gaussian random variable, given $f_{c,1}, \ldots, f_{c,n}$ with mean $\mathrm{E}\left[Y_s^{(s-n)}[1]\right] = 0$. The conditional variance can be found as:

$$\begin{aligned}
&\mathrm{var}\left(Y_s^{(s-n)}[1] \mid f_{c,1}, \ldots, f_{c,n}\right) \\
&= \mathrm{E}\left[\sum_{j=1}^{n} \int_0^T \int_0^T 4a^2 |H_{r,j}(f_0)|^2 \cos(2\pi f_0 t + \phi) \times \cos(2\pi f_0 \tau + \phi) \tilde{W}_{a,j}(t) \tilde{W}_{a,j}(\tau)\, dt\, d\tau\right] \\
&= 4a^2 \sum_{j=1}^{n} |H_{r,j}(f_0)|^2 \int_0^T \int_0^T \frac{1}{2}[\cos(2\pi f_0(t+\tau) + 2\phi) + \cos(2\pi f_0(t-\tau))] K_{\tilde{W}_{a,j}}(t-\tau)\, dt\, d\tau, \quad (17)
\end{aligned}$$

where $K_{\tilde{W}_{a,j}}(\cdot)$ is the autocovariance function of the filtered noise process $\tilde{W}_{a,j}(t)$ over the jth branch. The associated power spectral density can be written as $S_{\tilde{W}_{a,j}}(f) = \frac{N_a}{2}|H_{r,j}(f)|^2$. Here, let us define $\hat{H}_{r,j}(f)$ such that

$$|H_{r,j}(f)|^2 = |H_{r,j}(f_{c,j})|^2 \left[\hat{H}_{r,j}\left(\frac{f - f_{c,j}}{B}\right) + \hat{H}_{r,j}\left(\frac{f + f_{c,j}}{B}\right)\right], \quad (18)$$

where $B = f_0/2Q$ is the 3-dB bandwidth of $H_{r,j}(f)$. Thus, $\hat{H}_{r,j}(f)$ is the baseband representation of a sidelobe (sidelobes are symmetric) of $|H_{r,j}(f)|^2$, normalized to have a unit gain at DC frequency and a unit 3-dB bandwidth. Hence, the time-domain response of $|H_{r,j}(f)|^2$ is $2\cos(2\pi f_{c,j} t) B \hat{h}_{r,j}(Bt) |H_{r,j}(f_{c,j})|^2$, where $\hat{h}_{r,j}(t)$ is the inverse Fourier transform of $\hat{H}_{r,j}(f)$. Consequently, the autocovariance function of the $\tilde{W}_{a,j}$ can be written as

$$K_{\tilde{W}_{a,j}}(t) = N_a B H_{res}^2 \cos(2\pi f_{c,j} t) \hat{h}_{r,j}(Bt), \quad (19)$$

where H_{res} was introduced in (6). One can realize that the variance of white noise, filtered by the antenna response is $\sigma_{\tilde{W}_{a,j}}^2 = N_a B H_{res}^2$, where $B H_{res}^2$ can be viewed as the "energy" of the filter response. With this, we can evaluate the variance of the signal–noise cross component as:

$$\begin{aligned}
&\mathrm{var}\left(Y_s^{(s-n)}[1] \mid f_{c,1}, \ldots, f_{c,n}\right) \\
&= 2a^2 N_a \sum_{j=1}^{n} |H_{r,j}(f_0)|^2 H_{res}^2 \times \int_0^T \int_0^T [\cos(2\pi f_0(t-\tau)) \cos(2\pi f_{c,j}(t-\tau)) + \cos(2\pi f_{c,j}(t-\tau)) \cos(2\pi f_0(t+\tau))] \\
&\quad \times B \hat{h}_{r,j}(B(t-\tau))\, dt\, d\tau \\
&= 2a^2 N_a \sum_{j=1}^{n} |H_{r,j}(f_0)|^2 H_{res}^2 \left\{\int_0^T \int_0^T \frac{1}{2}[\cos(2\pi \times (f_{c,j} + f_0)(t-\tau)) + \cos(2\pi (f_{c,j} - f_0)(t-\tau))] \right. \\
&\quad \times B \hat{h}_{r,j}(B(t-\tau))\, dt\, d\tau + \int_0^T \int_0^T \frac{1}{2}[\cos(2\pi \\
&\quad \times ((f_{c,j} + f_0)t + (f_0 - f_{c,j})\tau)) + \cos(2\pi ((f_{c,j} - f_0)t
\end{aligned}$$

$$- (f_0 + f_{c,j})\tau))]B\hat{h}_{r,j}(B(t-\tau))\,dt\,d\tau \Bigg\} \quad (20)$$

$$\approx a^2 N_a \sum_{j=1}^{n} |H_{r,j}(f_0)|^2 H_{res}^2 \int_0^T \int_0^T B\hat{h}_{r,j}(B(t-\tau)) \times \cos(2\pi(f_{c,j} - f_0)(t-\tau))\,dt\,d\tau \quad (21)$$

$$\approx a^2 N_a \sum_{j=1}^{n} |H_{r,j}(f_0)|^2 H_{res}^2 \times \int_0^T \int_0^T B\hat{h}_{r,j}(B(t-\tau))\,dt\,d\tau \quad (22)$$

$$\approx T a_{eff}^2 N_a H_{res}^4, \quad (23)$$

where (21) follows since, (1) $f_0 \gg B$ and the high-frequency cosine terms have many cycles within the span of $\hat{h}_{r,j}(B(t-\tau))$; (2) the integrals of the cosines are inversely proportional to the frequencies and the high frequency cosines become negligible with respect to the integral of the cosine term at frequency $f_{c,j} - f_0$. Also, (22) follows when $f_{c,j} - f_0 \ll B$ for all j with high probability and the cosine term is almost constant at 1 for the span of $(t, \tau) \in (0, T)^2$ values that $\hat{h}_{r,j}(B(t-\tau))$ is non-zero.[4] Finally, (23) follows since $1/B \ll T$ and thus $\hat{h}_{r,j}(B(t-\tau))$ is identical to 0 for almost all pairs of $(t, \tau) \in [0, T]^2$ except for those that are very close to each other. Since the area under $\hat{h}_{r,j}(t)$ is 1, $B\hat{h}_{r,j}(B(t-\tau))$ acts as a unit impulse function $\delta(t-\tau)$.

As a result, given $f_{c,1}, \ldots, f_{c,n}$, $Y_s^{(s-n)}[1] \sim \mathcal{N}(0, T a_{eff}^2 N_a H_{res}^4)$. Note that, the strategy of increasing the transmit signal power, $a^2/2$, in order to reduce the time T to activate a node generally fails due to the signal–noise cross component, since the noise level is also amplified by the signal amplitude a.

(3) *Noise–noise cross component*: Regardless of whether there is an activation attempt in scheduling period $k = 1$, the noise–noise cross component will be observed at the output of the antenna. The contribution of the noise–noise cross component on the sample $Y_s[1]$ can be found as:

$$Y_s^{(n-n)}[1] = \int_0^T \tilde{W}_{a,j}^2(t)\,dt. \quad (24)$$

The noise–noise cross component has a non-zero mean: $E\left[Y_s^{(n-n)}[1] \mid f_{c,1}, \ldots, f_{c,n}\right] = T\sum_{j=1}^{n} \sigma_{\tilde{W}_{a,j}}^2 = TN_a BnH_{res}^2$. To find the variance, we note that $\tilde{W}_{a,j}^2$ has a power spectral density with a 3-dB bandwidth identical to $2B$. Since $1/2B \ll T$, for any pair $(t, \tau) \in (0, T)^2$, $K_{\tilde{W}_{a,j}^2}(t-\tau)$ is very close to 0, unless $t \approx \tau$. Due to the large bandwidth, we write $K_{\tilde{W}_{a,j}^2}(t-\tau) \approx \sigma_{\tilde{W}_{a,j}^2}^2 \delta(t-\tau)$. Consequently,

$$\begin{aligned} &\mathrm{var}\left(Y_s^{(n-n)}[1] \mid f_{c,1}, \ldots, f_{c,n}\right) \\ &= \sum_{j=1}^{n} \int_0^T \int_0^T K_{\tilde{W}_{a,j}^2}(t-\tau)\,dt\,d\tau \\ &\approx \sum_{j=1}^{n} \int_0^T \int_0^T \sigma_{\tilde{W}_{a,j}^2}^2 \delta(t-\tau)\,dt\,d\tau \\ &= \sum_{j=1}^{n} \int_0^T \int_0^T 2\sigma_{\tilde{W}_{a,j}}^2 \delta(t-\tau)\,dt\,d\tau \quad (25) \\ &= 2TB^2 N_a^2 n H_{res}^4. \quad (26) \end{aligned}$$

One cannot disregard the noise–noise cross component, since it can potentially be large due to the lack of a front-end filter.[5]

(4) *Thermal noise*: The contribution of thermal noise in the sample $Y_s[1]$ can be found as:

$$Y_s^{(T)}[1] = \int_0^T W_T(t)\,dt. \quad (27)$$

Clearly, $E\left[Y_s^{(T)}[1]\right] = 0$ and $\mathrm{var}\left(Y_s^{(T)}[1]\right) = T\frac{N_T}{2}$.

With the above observations, we can write the following conditional distributions for $Y_s[1]$, using a *Gaussian approximation* for the noise–noise cross component:
Given an activation attempt and $f_{c,1}, \ldots, f_{c,n}$,

$$Y_s[1] \sim \mathcal{N}\left(\underbrace{TH_{res}^2(a_{eff}^2/2 + nN_a B)}_{\mu_p}, \underbrace{T\left[N_a H_{res}^4(a_{eff}^2 + 2nB^2 N_a) + \frac{N_T}{2}\right]}_{\sigma_p^2}\right);$$

given *no* activation attempt and $f_{c,1}, \ldots, f_{c,n}$,

$$Y_s[1] \sim \mathcal{N}\left(\underbrace{TnH_{res}^2 N_a B}_{\mu_n}, \underbrace{Tn\left(2B^2 N_a^2 H_{res}^4 + \frac{N_T}{2}\right)}_{\sigma_n^2}\right).$$

In the subsequent analysis, we deal with the probability of two events: *unsuccessful activation attempt* and *false activation*. In the former, the activator attempts to activate a node, but the node remains inactive, whereas in the latter, the node goes active without an activation signal. We define the optimal detector [17,18] as the one that minimizes the *probability of unsuccessful activation attempt*, p_{ua}, subject to a given *probability of false activation*, p_{fa}. Since the signal–noise cross component is 0 without the activation signal, the total noise variance differs with and without the activation attempt as shown in Fig. 6. Thus, the optimal detector involves comparisons with multiple thresholds. We also define p_a as the prior probability for an activation attempt in any given activation period and probability of error as the total probability of an undesirable event: $p_e = p_a p_{ua} + (1 - p_a)p_{fa}$.

[4] Note that, in the other extreme, if the antenna has a very high Q-factor and $f_{c,j} - f_0 \gg B$ with high probability, the value of the integral decreases by a factor $B(f_{c,j} - f_0)^{-1}$.

[5] Note that the nanoantenna acts as a front-end filter to some extent. However, the bandwidth of the antenna response is fairly wide (depends on the Q factor) and it lets a significant amount of noise through.

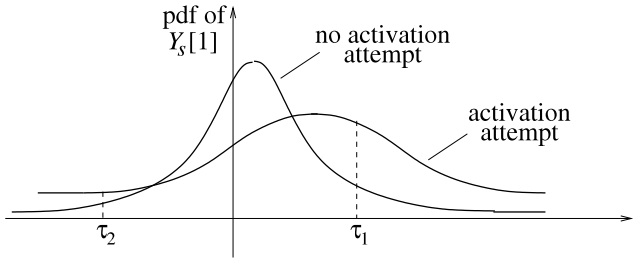

Fig. 6. The pdf of the detected signal under activation attempt and no activation attempt.

We will evaluate the performance in terms of the following parameters. Signal to acoustic noise ratio, $\text{SNR}_\text{a} \triangleq \frac{a^2}{2N_\text{a}B}$ and effective signal to acoustic noise ratio $\text{SNR}_\text{eff} \triangleq \frac{\text{E}\left[a_\text{eff}^2\right]}{2nN_\text{a}B}$, where the expectation is over the joint distribution of $f_{c,1}, \ldots, f_{c,n}$. In Fig. 7, we illustrate the ratio $\text{SNR}_\text{eff}/\text{SNR}_\text{a}$ for a single antenna, i.e., $n = 1$ as a function of the variance of the resonance frequency, normalized with respect to B^2, i.e., $\sigma_{f_0}^2/B^2$. One can observe that SNR_eff decays quickly with the resonance frequency variance. Indeed, if $\sigma_{f_0} = \sqrt{2}B$, then SNR_eff decays by half to $\text{SNR}_\text{a}/2$ from SNR_a.

In what follows, we illustrate the detector performance, and our main focus will be on the cases with moderate to large numbers of CNTs, i.e., $n \gg 1$. Consequently, our system will be *acoustic noise dominant* and the impact of the thermal noise becomes negligible. Furthermore, since for $n \gg 1$ we have $a_\text{eff}^2/n \approx \text{E}\left[a_\text{eff}^2\right]/n$ with high probability as given in (15), we can simplify our detection model as:
Given an activation attempt,

$$\frac{Y_s[1]-\mu_n}{\sigma_n} \sim \mathcal{N}\left(\sqrt{\frac{Tn}{2}}\text{SNR}_\text{eff},\, 1+\frac{\text{SNR}_\text{eff}}{B}\right);$$

given *no* activation attempt,

$$\frac{Y_s[1]-\mu_n}{\sigma_n} \sim \mathcal{N}(0,\,1).$$

Note that, here we neglect $TN_T/2$ in σ_n^2, since $n \gg 1$ and hence assume that the acoustic noise is the dominant noise source.

One can find that the maximum a posteriori decision rule activates the node if $Y_s[1] > \tau_1^{(\text{MAP})}$ or $Y_s[1] < \tau_2^{(\text{MAP})}$, where the thresholds $\tau_1^{(\text{MAP})}$ and $\tau_2^{(\text{MAP})}$ satisfy Eqs. (28) and (29) as given in Box I.

The *minimum* error probability (p_e associated with the maximum a posteriori detector) $p_\text{e}^{(\text{MAP})} = p_\text{a}p_\text{ua}^{(\text{MAP})} + (1-p_\text{a})p_\text{fa}^{(\text{MAP})}$, where

$$p_\text{ua}^{(\text{MAP})} = \Phi\left(\frac{\tau_1^{(\text{MAP})}-\mu_p}{\sigma_p}\right) - \Phi\left(\frac{\tau_2^{(\text{MAP})}-\mu_p}{\sigma_p}\right), \quad (30)$$

$$p_\text{fa}^{(\text{MAP})} = \Phi\left(\frac{\tau_2^{(\text{MAP})}-\mu_n}{\sigma_n}\right) + 1 - \Phi\left(\frac{\tau_1^{(\text{MAP})}-\mu_n}{\sigma_n}\right). \quad (31)$$

One can find evaluate $(\tau_i^{(\text{MAP})}-\mu_p)/\sigma_p$ for $i = 1, 2$ using $(\tau_i^{(\text{MAP})}-\mu_n)/\sigma_n$ as given in Eqs. (28) and (29) (which are given in Box I) as follows:

$$\frac{\tau_i^{(\text{MAP})}-\mu_p}{\sigma_p} = \left(\frac{\tau_i^{(\text{MAP})}-\mu_n}{\sigma_n} - \sqrt{\frac{nT}{2}}\text{SNR}_\text{eff}\right) \times \left(\sqrt{1+\frac{\text{SNR}_\text{eff}}{B}}\right)^{-1}. \quad (32)$$

Fig. 8 illustrates the performance of the nanoreceiver with multiple antennas. To obtain these curves, we chose the parameters of the system as $f_0 = 15$ MHz, $Q = 500$ (i.e., $B = 15$ kHz), $p_\text{a} = 10^{-3}$, and $\sigma_{f_0}^2/B^2 = 0.1$. In Fig. 8(a), we illustrate the probability of error as a function of the number of antennas for various values of SNR_a for $T = 1$ s. Similarly, in Fig. 8(b), we illustrate the probability of error as a function of SNR_a for various values of n for $T = 1$ s. Firstly, one can observe a *phase transition* phenomenon in the detection performance of our system. For a given SNR_a, there is a threshold for the number of antennas below

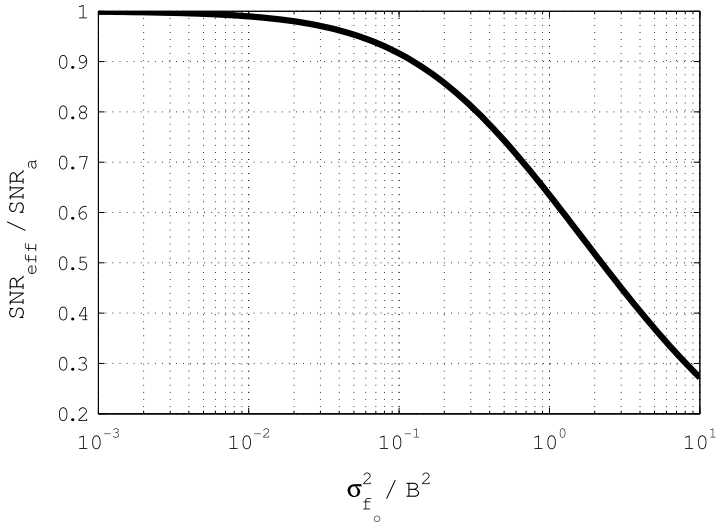

Fig. 7. $\text{SNR}_\text{eff}/\text{SNR}_\text{a}$ vs. $\sigma_{f_0}^2/B^2$.

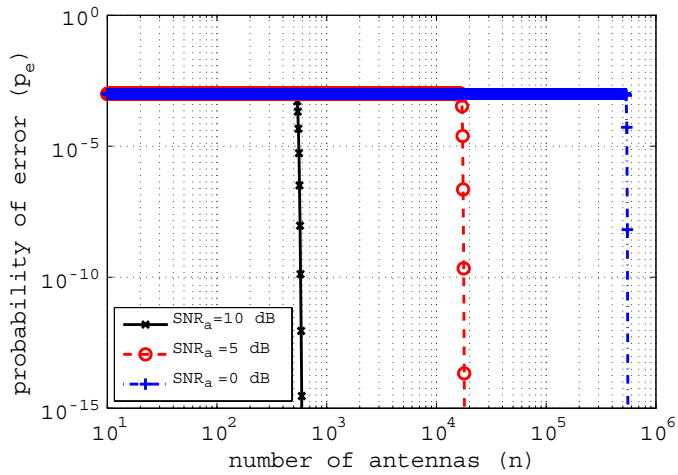

(a) p_e vs. n.

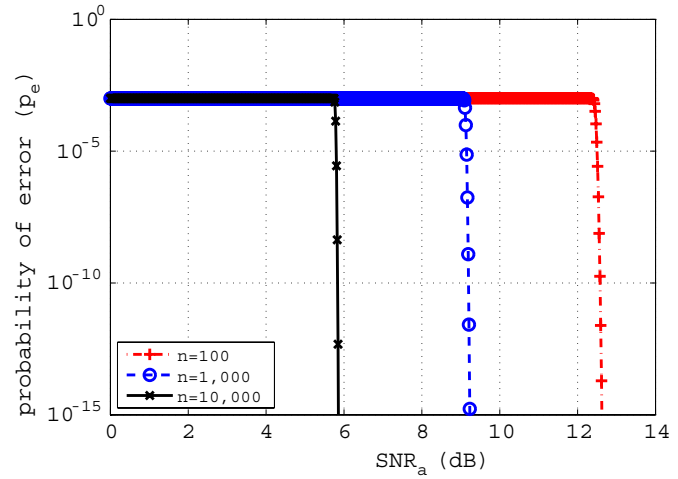

(b) p_e vs. SNR_a.

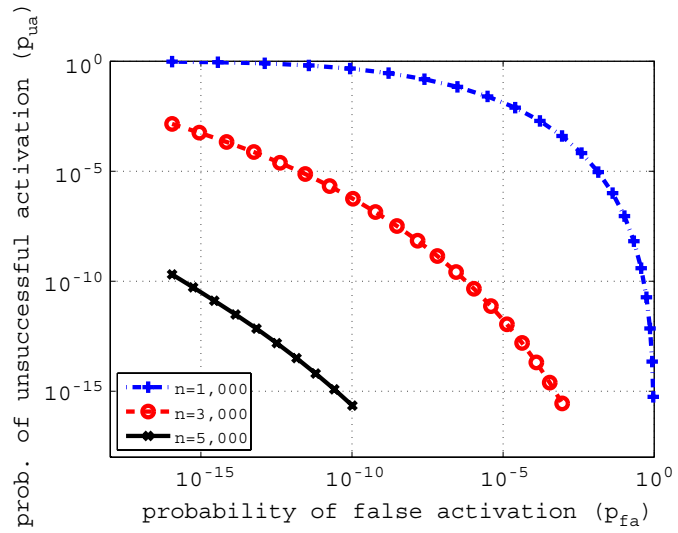

(c) p_{ua} vs. p_{fa}.

Fig. 8. System performance and various tradeoffs are illustrated for our nanoreceiver.

which the detection error probability is high and above which the detection probability is negligibly small. For instance, if $\text{SNR}_a = 10$ dB, proper activation is not possible in $T = 1$ s unless the number of CNTs $n > 20$. On the other

$$\frac{\tau_1^{(\mathrm{MAP})}-\mu_n}{\sigma_n}=\sqrt{\frac{nT}{2}}B\left(-1+\sqrt{\left(1+\frac{\mathrm{SNR}_{\mathrm{eff}}}{B}\right)\left(1+\frac{2}{T\mathrm{SNR}_{\mathrm{eff}}}\left(\frac{1}{\mathrm{SNR}_{\mathrm{eff}}}+\frac{1}{B}\right)\log\left[\left(\frac{1}{p_{\mathrm{a}}}-1\right)^2\left(1+\frac{\mathrm{SNR}_{\mathrm{eff}}}{B}\right)\right]\right)}\right), \quad (28)$$

$$\frac{\tau_2^{(\mathrm{MAP})}-\mu_n}{\sigma_n}=\sqrt{\frac{nT}{2}}B\left(-1-\sqrt{\left(1+\frac{\mathrm{SNR}_{\mathrm{eff}}}{B}\right)\left(1+\frac{2}{T\mathrm{SNR}_{\mathrm{eff}}}\left(\frac{1}{\mathrm{SNR}_{\mathrm{eff}}}+\frac{1}{B}\right)\log\left[\left(\frac{1}{p_{\mathrm{a}}}-1\right)^2\left(1+\frac{\mathrm{SNR}_{\mathrm{eff}}}{B}\right)\right]\right)}\right) \quad (29)$$

Box I.

hand, if $n > 20$, the probability of activation error is below 10^{-15}. Examining Fig. 8(b), one can observe that a factor of 10 increase in the number of antennas is necessary for every $\sim$ 3.5 dB decrease in $\mathrm{SNR_a}$ at a given probability of error.

In Fig. 8(c), we illustrate the *receiver operating characteristics* (ROC); i.e., minimum p_{ua} achievable by our nanoreceiver for a given p_{fa} à la Neyman–Pearson criterion [17] for various values of the number of antennas for a fixed $T = 0.1$ s and $\mathrm{SNR_a} = 0$ dB. To plot these curves, we used the pair of thresholds $\tau_1^{(\mathrm{NP})}$ and $\tau_2^{(\mathrm{NP})}$, and calculated the associated values of p_{ua} and p_{fa}, based on the decision rule, "activate node if $Y_s[1] > \tau_1$ or $Y_s[1] < \tau_2$" and remain inactive otherwise. The Neyman–Pearson thresholds $\tau_1^{(\mathrm{NP})}$ and $\tau_2^{(\mathrm{NP})}$ turn out to be identical to $\tau_1^{(\mathrm{MAP})}$ as in (28) and $\tau_2^{(\mathrm{MAP})}$ as in (29) respectively, evaluated as the value of p_{a} is varied in [0, 1]. Note that, this does not imply that the values of p_{ua} and p_{fa} depend on the probability of activation at all. Here, p_{a} is merely a parameter that gives us the Neyman–Pearson thresholds to find the minimum p_{ua} subject to a given p_{fa}. The ROC is sketched by plotting (30) vs. (31) as the thresholds are varied using p_{a} as described above.

Fig. 8(c) shows that our nanoreceiver is highly reliable. With $n = 3000$ and an $\mathrm{SNR_a}$ as low as 0 dB, one can achieve a $p_{ua} = 10^{-7}$ at a $p_{fa} = 10^{-9}$. Note that, at this p_{fa} and T pair, even over a *month* of continuous operation, the probability of false activation of our node remains below 10^{-2}. Even with such a conservative selection, it is possible to achieve a probability of unsuccessful activation as low as 10^{-7} during the entire operation.

We just illustrated that, even with our simple nanoreceiver, the activation of a node with very low probability of error is possible with reasonably short activation signals and at values of overall signal to noise ratio as low as 3 dB, which can be further reduced by 3 dB, every time the number of antennas is doubled. Moreover, our nanoreceiver is reliable: it can be designed to operate over months without a false activation event and at the same time to achieve fairly low probabilities of unsuccessful activation, even with activation periods of as low as a few seconds. Lastly, the receiver performance is independent of the random phase, ϕ, of the carrier signal (due to the square-law device). Hence, our nanoreceiver avoids the complex circuitry for phase recovery.

Example: Suppose, our nanoreceiver is used as a particle detector, as described in Section 2.3. The detector has n CNTs in a $\sqrt{n} \times \sqrt{n}$ square region. We divide the detector into sectors, so that the entire region has $\sqrt{k} \times \sqrt{k}$ sectors, each of which contains n/k CNTs. Each sector has a separate nanoreceiver of its own and is capable of detecting a particle, independently from other sectors. However, since there is only one nanodetector per sector, only the presence or absence of one or more particles can be detected. Clearly, there is an error–resolution tradeoff: as the sector size increases, the probability of detection error decreases within each sector due to the increased number of antennas in that sector, whereas the position accuracy and the number of particles that can be detected can only be achieved at a resolution, inversely proportional to the sector size.

We illustrate this tradeoff in Fig. 9. The parameters of the system are chosen to be $f_0 = 15$ MHz, $Q = 500$ (i.e., $B = 15$ kHz), $p_{\mathrm{a}} = 10^{-3}$, and $\sigma_{f_0}^2/B^2 = 0.1$, and $\mathrm{SNR_a} = 13$ dB. The left ordinate shows the probability of error and the right ordinate shows the size of a sector, which is inversely proportional to the resolution. Clearly, a more accurate and sharper detection constraint requires smaller sector sizes, which come at cost of higher probabilities of detection error.

Finally, we note that carrier frequency mismatch is an important factor that affects the system's performance. In the above analyses, we assumed that the carrier frequency is identical to the mean resonance frequency of the nanoantennas, i.e., f_0. In practice, it may be difficult to perfectly estimate this value, and hence, there may be a mismatch between the carrier frequency and the mean resonance frequency. Suppose the carrier frequency is $f_0 + \Delta f_0$, where Δf_0 is the amount of mismatch.

In Fig. 10, we plot the ratio $\mathrm{SNR_{eff}}/\mathrm{SNR_a}$ for a single-antenna receiver, as a function of $\Delta f_0/B$, the mismatch normalized with respect to the bandwidth of the antenna response for various values of $\sigma_{f_0}^2/B^2$. There are two things notable in this figure. First, one can observe a sharp decrease in the effective SNR with increased amount of mismatch. Secondly, the sensitivity of $\mathrm{SNR_{eff}}$ with respect to frequency mismatch is smaller, if $\sigma_{f_0}^2$ is higher. Furthermore, as Δf_0 gets larger, $\mathrm{SNR_{eff}}$ can even be greater for larger values of $\sigma_{f_0}^2$, compared to the smaller values. This extraordinary behavior can be explained as follows. If $\sigma_{f_0}^2$ is low, all resonance frequencies will be very close to f_0 with high probability. Thus, if the frequency mismatch is high, all the antennas will uniformly have a very low signal component. However, higher values of $\sigma_{f_0}^2$ lead to a larger spread of resonance frequencies and there is a higher probability that some of the antennas align with the carrier frequency. This kind of "hedging" improves the performance considerably and makes the system more robust with respect to carrier frequency fluctuations.

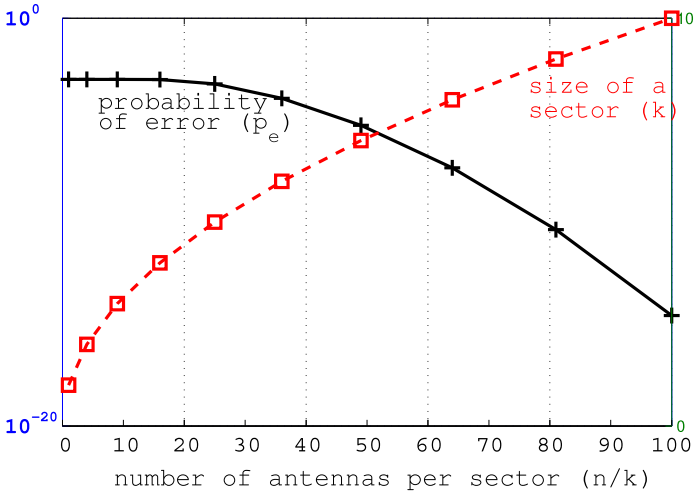

Fig. 9. Probability of error and resolution are illustrated vs. the number of antennas.

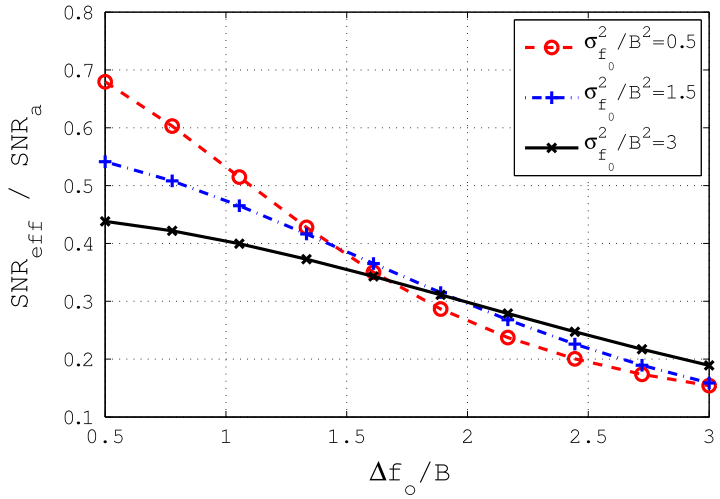

Fig. 10. SNR_{eff}/SNR_a as a function of $\Delta f_0/B$.

These results illustrate the feasibility of individual node activation in real environments using simple and realizable, and yet reliable nanoreceivers with multiple nanoantennas. However, the performance is highly sensitive with respect to the nanoantenna parameters and possible imperfections due to frequency and timing mismatches.

We would like to finalize this section by noting that one can achieve multiple tasks per node by waiting for multiple activation periods and interpreting sequences of pulses. Taking this idea one step further, we can actually use the nanoreceiver for *digital data communication*. Indeed, the reciprocal, $1/T$, of the activation period of the system can be viewed as the *data rate* of the communication system at the associated probability, p_e, of error. For instance, a rate of 1 bit/sec is achievable at a $p_e < 10^{-10}$ at a signal to noise ratio of 6 dB using a nanoreceiver with 10,000 CNTs. Data communication enables the possibility of more complex tasks for each node.

5. Conclusions

In this paper, we introduced several system-level design possibilities based on CNT-based RF receivers. Moreover, we provided a communication-theoretical analysis of the basic building block of such systems involving multiple CNT-based RF receivers. Our analysis has revealed that, while the performance of individual CNT-based receivers is limited, such limitations can easily be overcome through the use of multiple CNTs in the same receiver system. We showed that using multiple CNT antennas led to an almost proportional increase in the performance. Given that one can grow thousands of CNT antennas on the same substrate, in the long run, multi-CNT-based rf receivers have the potential to replace classical rf receivers in wireless communications. Similarly, these properties are expected to lend previously unimaginable communication capabilities to nanoscale devices and systems.

Admittedly, this line of research is still in its infancy and much remains to be done. As an immediate first step, we aim to validate our theoretical findings through real-life implementations. Moreover, any nanoscale system is composed of several components that interact very closely. Interactions of nanoscale components in the same design need further scrutiny. Reliability of communication is also another point that we will investigate further.

References

[1] I. Akyildiz, C.B.F. Brunetti, Nanonetworks: a new communication paradigm, Computer Networks 52 (2008) 2260–2279.
[2] B. Atakan, O.B. Akan, Carbon nanotube-based nanoscale ad hoc networks, IEEE Communications Magazine (June) (2010) 129–135.
[3] J. Aylott, Optical nanosensors an enabling technology for intracelular measurements, Analyst (2003) 309–312.
[4] B. Behkam, M. Sitti, Bacterial flagella-based propulsion and on/off motion control of microscale objects, Applied Physics Letters 90 (January) (2007).
[5] Y. Cheng, O. Zhou, Electron field emission from carbon nanotubes, Comptes Rendus Physique (4) (2003) 1021–1033.
[6] D. Dragoman, M. Dragoman, Tunneling nanotube radio, Journal of Applied Physics 104 (October) (2008).
[7] E. Drexler, Nanosystems: Molecular Machinery, Manufacturing, and Computation, John Wiley and Sons Inc., 1992.
[8] R. Freitas, Nanotechnology, nanomedicine and nanosurgery, International Journal of Surgery 3 (November) (2005) 243–246.
[9] R. Freitas, Pharmacytes: an ideal vehicle for targeted drug delivery, Journal of Nanoscience and Nanotechnology 6 (September) (2006) 2769–2775.
[10] M. Gregori, I. Akyildiz, A new nanonetwork architecture using flagellated bacteria and catalytic nanomotors, IEEE Journal on Selected Areas in Communications 28 (May) (2010) 612–619.
[11] D.J. Griffiths, Y. Li, Charge density on a conducting needle, American Journal of Physics 64 (1996) 706–714.
[12] K. Jensen, J. Weldon, H. Garcia, A. Zettl, Nanotube radio, Nano Letters 7 (November) (2007) 3508–3511.
[13] J.M. Jornet, I. Akyildiz, Channel capacity of electromagnetic nanonetworks in the terahertz band, in: Proceedings of IEEE ICC 2010, May 2010.
[14] E.C. Koksal, E. Ekici, A nanoradio architecture for interacting nanonetworking tasks, Elsevier Nano Communication Networks Journal 1 (March) (2010) 63–75.
[15] M. Pierobon, I. Akyildiz, A physical channel model for molecular communication in nanonetworks, IEEE Journal on Selected Areas in Communications 28 (May) (2010) 602–611.
[16] P. Poncharal, Z.L. Wang, D. Ugarte, W.A. de Heer, Electrostatic deflections and electromechanical resonances of carbon nanotubes, Science 283 (March) (1999) 1513–1516.
[17] H.V. Poor, An Introduction to Signal Detection and Estimation, 2nd ed., Springer, New York, 1994.
[18] J.G. Proakis, Digital Communications, 3rd ed., McGraw-Hill, New York, 1995.
[19] J. Weldon, K. Jensen, A. Zettl, Nanomechanical radio transmitter, Physica Status Solidi B 245 (October) (2008) 2323–2325.

C. Emre Koksal received his B.S. degree in electrical engineering from the Middle East Technical University, Ankara, Turkey, in 1996, and his S.M. and Ph.D. degrees from the Massachusetts Institute of Technology (MIT), Cambridge, in 1998 and 2002, respectively, in electrical engineering and computer science. He was a Post doctoral Fellow in the Networks and Mobile Systems Group in the Computer Science and Artificial Intelligence Laboratory, MIT, until 2003 and a Senior Researcher jointly in the Laboratory for Computer Communications and the Laboratory for Information Theory at EPFL, Switzerland, until 2006. Since then, he has been an Assistant Professor in the Electrical and Computer Engineering Department, Ohio State University, Columbus. His general areas of interest are wireless communication, computer networks, information theory, stochastic processes, and financial economics.

Eylem Ekici received his B.S. and M.S. degrees in computer engineering from Bogazici University, Istanbul, Turkey, in 1997 and 1998, respectively. He received his Ph.D. degree in electrical and computer engineering from Georgia Institute of Technology, Atlanta, in 2002. Currently, he is an associate professor in the Department of Electrical and Computer Engineering of The Ohio State University. His current research interests include cognitive radio networks, nanoscale networks, vehicular communication systems, and wireless sensor networks, with a focus on routing and medium access control protocols, resource management, and analysis of network architectures and protocols. He is an associate editor of IEEE/ACM Transactions on Networking, Computer Networks Journal (Elsevier), and ACM Mobile Computing and Communications Review.

Siddharth Rajan is Assistant Professor in the Electrical and Computer Engineering and Material Science and Engineering departments at The Ohio State University. He received undergraduate degrees in physics and electrical engineering from Birla Institute of Technology and Science, Pilani, India in 2001, and M.S. and Ph.D. degrees in electrical and computer engineering from University of California, Santa Barbara in 2006. His research interests include high-performance electronic devices, nanoscale semiconductor physics, molecular beam epitaxy, and new materials.